

Reactor-based Search for Axion-Like Particles using CsI(Tl) Detector

S. Sahoo^a, S. Verma^a, M. Mirzakhani^a, N. Mishra^a, A. Thompson^b, S. Maludze^a, R. Mahapatra^a, M. Platt^a

^a*Department of Physics and Astronomy, Texas A&M University , 578 University Dr, College Station, 77840, TX, US*

^b*DEPARTMENT OF PHYSICS & ASTRONOMY, Northwestern University, 2145 Sheridan Road, Tech F165 Evanston, Illinois, 60208-3112, USA*

Abstract

Null results for WIMP dark matter have led to increased interest in exploring other dark matter candidates, such as Axions and Axion-Like Particles (ALPs), which also helps in answering the strong CP problem. This experiment achieved a sub-100 DRU (differential-rate-unit, expressed in counts/keV/kg/day) background in the MeV region of interest by employing a combination of active and passive veto techniques. Such a low background facilitates the search for ALPs with axion-photon coupling $g_{a\gamma\gamma} > 10^{-6}$ and axion-electron coupling $10^{-8} < g_{aee} < 10^{-4}$ in the 1 keV to 10 MeV mass range. This indicates that the experiment has the capability to constrain the unexplored cosmological triangle in the ALP-photon parameter space for ALPs in the MeV mass range.

1. Introduction

Various astrophysical observations based on the behavior of galaxies in the galaxy clusters [1, 2], rotational velocity curves of stars in galaxies [3], gravitational lensing [4] etc.. have confirmed the existence of non-luminous matter in the universe or the so-called dark matter. About 83% of the matter content of the universe is in the form of dark matter. Among Dark Matter Candidates, Axions have dual motivations, besides being one of the candidates for dark matter in the Universe, they also solve the strong CP problem of the Standard Model.

Various methods have been employed to explore the parameter space of the ALP, focusing on its couplings to photons, electrons, and nucleons according to its mass. These methods include helioscopes such as CAST [5, 6, 7]; haloscopes like Abracadabra [8, 9], ADMX [10, 11], CASPEr [12], and HAYSTAC [13, 14]; light-shining-through-walls experiments like ALPSII [15]; and interferometry[16, 17] approaches such as ADBC [18] and DANCE [19]. Additionally, current and proposed beam dump and fixed target experiments, including FASER [20], LDMX [21, 22], NA62 [23], SeaQuest [24] and SHiP [25], have been utilized. Hybrid approaches combining beam dump and helioscope techniques, like PASSAT [26], as well as dark matter experiments such as XENON [27, 28], SuperCDMS [29], and PandaX [30], also contribute to this search.

In this experiment, we focus on the reactor-based search for Axions/Axion-Like Particles (ALPs). These investigations have the ability to explore MeV mass range ALPs by using the large number of photons generated in the nuclear reactor core. Once the axions/ALPs are produced at the reactor core [31], if they travel unimpeded to the detection site, they can scatter off the detector material via inverse Primakoff or inverse Compton-like scatterings to produce photons or decay into di-photons or electron-positron pairs which are then detected using CsI(Tl) scintillator detectors providing strong constraints on ALP-photon coupling.

This paper is organized as follows. Section 2 covers the

theoretical framework of the experiment, detailing the production of ALPs at the reactor, their detection by our detector, and the overall sensitivity of the process. Section 3 outlines the experimental setup near the reactor, providing information about the reactor, detector, data acquisition process, sources of background, and different shielding techniques. In section 4, the results of the experiments are analyzed. Then in the last section we have added the exclusion plot for ALPs search in the desired region. It also goes through the future improvements for the experiment and extending its reach to other unexplored region of the parameter space.

2. Theoretical Framework

This experiment is being carried out at a TRIGA-type nuclear reactor which is made up of a low-enriched uranium core operating at a power of 1 MW situated at the Nuclear Science Center (NSC) at Texas A&M university. It produces 9×10^{11} photons/cm²/s [32] through fission processes which can then scatter off the reactor material and produce ALPs [31] that may get detected by CsI(Tl) scintillator detectors if they decay to photon or electrons [33].

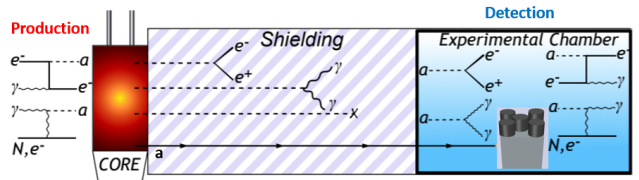


Figure 1: Schematic showing the experimental strategy for the production and detection of ALPs at the reactor. ALPs are generated at the reactor core via scattering with reactor material and detected using a CsI(Tl) detector assembly, as shown in the schematic. The ALP could decay and evade detection inside the shielding, depending on their lifetime (dashed lines) [31].

2.1. ALP Production Mechanism at the Reactor

Fission, capture processes in fuel and other materials, decay of fission products, inelastic scattering in the fuel, and decay of capture products are responsible for producing a large number of photons in the reactor core [34]. Once produced, these photons can interact with the reactor material which in our case is ^{235}U , and ALPs are produced at the reactor core via Primakoff process, Compton-like process and nuclear de-excitation. For details regarding nuclear de-excitation process, please refer to [35, 36]. Fig. 2 shows all these three processes for the photon-induced production of ALPs at the reactor.

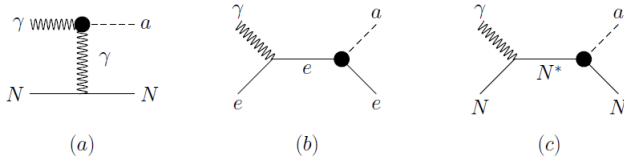


Figure 2: Mechanisms for producing ALPs at the reactor facility. (a) represents Primakoff process ($\gamma + A \rightarrow a + A$, where A is the atomic target), (b) represents Compton-like process ($\gamma + e^- \rightarrow a + e^-$) and (c) represents nuclear de-excitation ($\gamma + N \longleftrightarrow N^* \rightarrow a + N$) [35].

We will focus on the generic model where ALP can be produced either through photon coupling or via electron coupling and follow through it to calculate the sensitivities for ALP-photon or ALP-electron couplings [33].

2.2. ALP Detection Mechanism at the Reactor

Once ALPs are produced, it can be detected through the production of photons at the detection site via the inverse Primakoff process $a + A \rightarrow \gamma + A$ (where A is the atomic target). It can also interact with the electrons through inverse Compton-like process $a + e^- \rightarrow \gamma + e^-$ to produce photons and it can also decay to two photons or e^-/e^+ inside the detector material depending on its lifetime. This is illustrated in Fig. 1. The detector is housed in a hermetic shielding to further reduce the gamma background. Nuclear absorption $a + N \longleftrightarrow N^* \rightarrow \gamma + N$ can also serve as the detection for ALPs at the detector site [33].

2.3. Sensitivity Analysis

To a larger extent, we will follow minimal ALP assumption in a way that allows ALP-SM coupling that follows the same processes for the production and detection of ALPs [31]. As can be seen from Fig. 2(a), the Primakoff process takes place via t-channel virtual photon exchange, and the rate is determined by the strength of the coupling $g_{a\gamma\gamma}$ [31]. The differential cross-section for the production of ALPs via Primakoff process in the reactor core is given by,

$$\frac{d\sigma_P^P}{dcos\theta} = \frac{1}{4} g_{a\gamma\gamma}^2 \alpha Z^2 F^2(t) \frac{|\bar{p}_a|^4 \sin^2 \theta}{t^2} \quad (1)$$

where $t = (p_1 - k_1)^2 = m_a^2 + E_a(E_a - |\bar{p}_a| \cos \theta)$ is the square of the four-momentum transfer, Z is the atomic number of the target nucleus, α is Fine structure constant, F(t) is the form

factor, $|\bar{p}_a|$ is the magnitude of the ALP's outgoing three-momentum, and E_γ is the incident photon energy. Notice that the production cross-section is enhanced by the coherency factor Z^2 which makes our experiment more sensitive to ALP production and detection via the Primakoff channel as compared to other channels.

The differential cross section for the inverse Primakoff process has the same relation as in Eq. 1, with the front-factor 1/4 becoming 1/2 as in this case the initial spin states include a spin-0 ALP rather than a spin-1 photon.

ALPs can also decay into two photons inside the detector volume as shown in Fig. 1 with the decay-width given by,

$$\Gamma(a \rightarrow \gamma\gamma) = \frac{g_{a\gamma\gamma}^2 m_a^3}{64\pi} \quad (2)$$

which combined with the ALP kinetic energy, fixes the decay length.

ALP signal rate via the inverse Primakoff process is estimated by the convolution of the detection rate with the reactor photon flux as follows,

$$S(\text{scattering}) = m_{det} \Delta t N_T \sigma_P^d \frac{1}{4\pi l_d^2} \int dE_\gamma \frac{dN_\gamma}{dE_\gamma} \frac{\sigma_P^P}{\sigma_{SM}} P_{surv}^\gamma \quad (3)$$

where, m_{det} is the mass of the detector in kg, Δt is the data-taking time, N_T is the number of target atoms, σ_P^d is the Inverse Primakoff scattering cross-section, l_d is the core-detector distance, $dE_\gamma \frac{dN_\gamma}{dE_\gamma}$ is the number of photons at the reactor core, $\frac{\sigma_P^P}{\sigma_{SM}}$ is the branching ratio for ALP production in the core via the Primakoff process with respect to all other standard model processes and P_{surv}^γ is the ALP survival probability after they have traveled all the way from the reactor core to the detector without decaying,

$$P_{surv}^\gamma = \exp\left(-\frac{l_d}{v_a \tau_a^\gamma}\right) \quad (4)$$

where, v_a is the axion velocity and $\tau_a^\gamma = \frac{E_a}{m_a} \frac{1}{\Gamma(a \rightarrow \gamma\gamma)}$ is the axion decay lifetime.

Similarly, for the decay of axion into two photons, the ALP signal rate is estimated as follows,

$$S(\text{decay}) = \Delta t N_T \sigma_P^d \frac{A}{4\pi l_d^2} \int dE_\gamma \frac{dN_\gamma}{dE_\gamma} \frac{\sigma_P^P}{\sigma_{SM}} P_{surv}^\gamma P_{decay}^\gamma \quad (5)$$

where A is the detector transverse area, P_{decay}^γ is the axion decay probability inside the detector volume,

$$P_{decay}^\gamma = \exp\left(-\frac{l_d}{v_a \tau_a^\gamma}\right) \left[1 - \exp\left(-\frac{\Delta l}{v_a \tau_a^\gamma}\right)\right] \quad (6)$$

where Δl is the fiducial detector length. Notice that the axion decay width in its rest frame given by Eq. 2 varies as m_a^5 as the coupling constant varies as m_a . Since the decay lifetime varies inversely to the decay width, this results in a rapid loss in

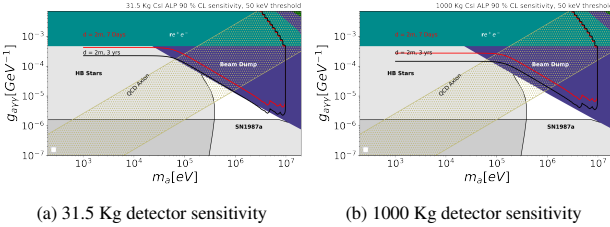


Figure 3: Projected sensitivity for the axion-photon coupling for future upgrades as mentioned. (a) for the current 5×5 setup of 25 CsI(Tl) crystals with approximately 31.5 kg active detector mass kept at a distance of ~ 2 m from the reactor core for 7 days and 3 years of exposure. (b) for a 1-ton CsI(Tl) setup kept at a distance of ~ 2 m from the reactor core for 7 days and 3 years of exposure.

sensitivity to light axions whose decay exceeds the experimental flight path. Thus heavier axions are sensitive to decay limits which we will show later while discussing the axion-photon sensitivity [33].

Similar analysis can be done for axion production and detection via Compton-like processes and decay into electron-positron pair and for the nuclear de-excitation and absorption case. The detailed calculation can be found in the references [31, 35, 36].

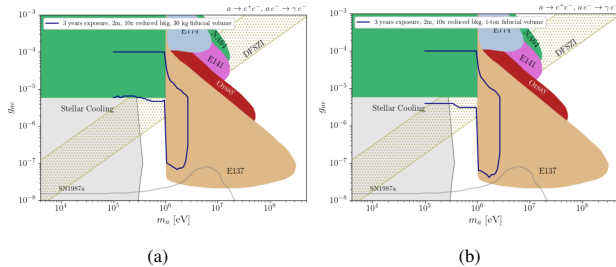


Figure 4: Projected sensitivity of the axion-electron coupling for the future upgrades as mentioned. (a) for the current 5×5 setup of 25 CsI(Tl) crystals with approximately 31.923 kg active detector mass kept at a distance of ~ 2 m from the reactor core with $10\times$ reduced background for 3 years of exposure. (b) for a 1-ton CsI(Tl) setup kept at a distance of ~ 2 m from the reactor core with $10\times$ reduced background for 3 years of exposure [33].

3. Experimental set-up

This section will explain the specific details regarding the reactor, detector, different types of internal or external backgrounds and shielding methods to limit the backgrounds. We will also mention the data acquisition process at the end.

3.1. Reactor (gamma source)

As mentioned in Section 2, this is a 1MW TRIGA (Testing, Research, Isotopes, General Atomics) reactor which uses low enriched ^{235}U as its fuel elements. This reactor also has a movable core which can give us higher proximity to the core up-to 2m. It produces ample amount of photons with flux $9 \times 10^{11}/cm^2/\text{sec}$ with end point energy 10MeV . Attached plot represents the photon flux coming from the reactor [32].

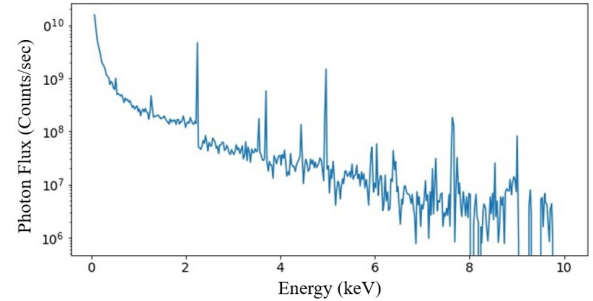


Figure 5: Photon flux coming from the reactor.

3.2. Detector

The proposed experimental setup utilizes around 25 thallium doped cesium iodide (CsI(Tl)) scintillators (each weighing 3.52 kg and measuring $2'' \times 2'' \times 12''$ in dimension) arranged in compact 5×5 manner as shown in Fig. 6. CsI(Tl) has been chosen due to its high light yield (54000 photons per MeV gamma energy deposition), high density, and less hygroscopic nature compared to other scintillators (which makes it suitable to be used under normal atmospheric conditions).

8	7	6	5	4
9	20	21	22	3
10	19	24	23	2
11	18	17	16	1
12	13	14	15	0

Figure 6: Detector for the experiment. 25 CsI(Tl) crystals arranged in 5×5 compact detector. Inner 9 crystals constitute the fiducial volume for the detector while outer 16 crystals are used as active-veto for the background.

Being one of the densest scintillators available with the combination of good light yield and ease of handling, they suit very well as a detector material to search for ALPs via Primakoff process due to Z^2 enhancement (shown in Eq. 1). Each CsI(Tl) crystal is wrapped with a Teflon tape for better total internal reflection of the scintillating photons (550 nm wavelength) and then a layer of thin aluminized mylar film is wrapped which reflects external light. One end of these crystals is coupled to conventional EMI photomultiplier tubes (PMT) for light collection [33].

3.2.1. Characterization of CsI(Tl)

Various radioactive sources such ^{22}Na , ^{137}Cs , ^{60}Co , ^{57}Co , ^{241}Am etc. have been used to characterize the performance of CsI(Tl) crystals which are being used in this experiment.

The calibration for different gamma energies from 60 KeV to 1.3 MeV is linear for CsI(Tl) as shown in Fig. 7a which makes it even more desirable as a gamma detector. The lowest experimental threshold is around 60 KeV for the full-size CsI(Tl) crystal as tested with 60 KeV gammas from ^{241}Am source. The percentage energy resolution at different energies is

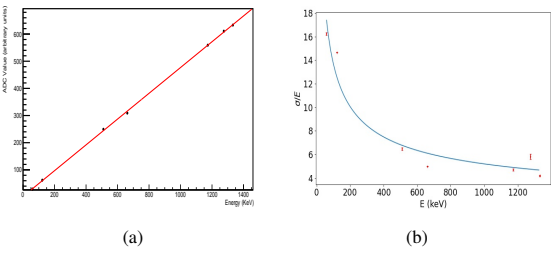


Figure 7: (a) Calibration curve obtained with different radioactive sources using CsI(Tl) crystal showing linearity. (b) Percentage energy resolution ($\sigma/E \%$) of CsI(Tl) using various radioactive sources [33].

shown in Fig. 7b, which follows the expected theoretical curve [33].

3.3. Sources of backgrounds

As we are dealing with a rare event search experiment, understanding the source of background radiation using the compact CsI(Tl) setup and lowering the background is critical for axion search. Dominating background radiation can emerge from natural radioactivity, radio-active impurities in the detector material and shielding, cosmic rays and neutrons from the reactor (since this is a reactor-based experiment), etc.. Some of these sources of background are presented in detail here [33].

3.3.1. Environmental Radioactivity

Element	Half life	Decay Product	Max Energy (MeV)
^{238}U	10^9 yrs	α	7.8
		β^-	5.48
		γ	1.76 (mostly)
^{232}Th	10^{10} yrs	α	8.95
		β^-	5
		γ	2.6 (mostly)
^{40}K	10^9 yrs	β^-	1.31
		γ	1.5

Environmental gamma radiation that might cause background in CsI(Tl) detectors comes from three sources: primordial, cosmogenic, and anthropogenic[37]. Primordial isotopes have a half-life of $\geq 10^9$ years. ^{238}U , ^{232}Th and ^{40}K are primordial sources which are prevalent in the environment. A number of gammas are emitted with different energies and intensities during the decay of ^{238}U and ^{232}Th isotopes to their stable states. These gammas from ^{238}U and ^{232}Th chain along with the 1460 KeV gammas from the decay of ^{40}K are the main contributors to the external natural background radiation in this experiment. One key thing to note is that the maximum gamma energy restricts at 2.6 MeV from natural radioactivity.

3.3.2. Cosmic-rays

Cosmic muons which have a flux of around 1 muon/cm²/minute at sea level are minimum ionizing particles and deposit (dE/dx) ~ 2 MeV/g/cm² while passing through a material. Since the

density of CsI(Tl) is 4.51 g/cm³ and the CsI(Tl) crystals are kept vertically, so assuming vertical muons, they will travel through approximately 30 cm of CsI(Tl) crystal depositing ~ 270 MeV of energy in it which is much beyond the region of interest and will most likely lead to saturated events in the digitizer. Even for horizontal configuration, considering 5 cm thickness of CsI(Tl), the deposited energy by muons is ~ 45 MeV which is still beyond the region of interest. Thus, cosmic muons are not a critical source of background for this experiment.

3.3.3. Internal Radioactivity of CsI(Tl)

The internal background of CsI(Tl) has been measured using an HPGe detector which helps us to have a robust internal background model. Fig. 8 shows the HPGe spectrum for CsI(Tl) sample and the background with major gamma peaks identified. ^{214}Bi , ^{134}Cs , ^{137}Cs and ^{40}K are the major internal backgrounds found using the HPGe detector. Some of the ^{40}K background (in which 1460 KeV gammas are emitted after electron capture [38]) is also contributed due to the surrounding lead/concrete shielding.

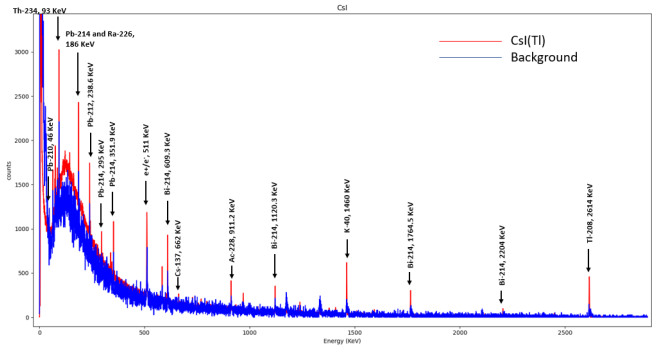


Figure 8: HPGe spectrum of the CsI(Tl) sample and the background spectrum with major gammas peaks [33].

3.4. Passive and Active Shielding Techniques

Background reduction is the goal for all the rare search experiments. As it has been shown here, with the modest setup of 25 CsI(Tl) crystals and the combination of active and passive shielding/veto techniques, we are able to reach sub-100 DRU (differential rate unit expressed in counts/KeV/Kg/day) background in the MeV scale gamma energy range [33].

Passive Shielding:

For passive shielding, we have used 1/4" of copper, 4" of lead, and water bricks as shown in Fig. 9. We found that copper and water bricks do not make much difference since our region of interest lies in 100 KeV to a few MeV and thus in the later experimental runs, only 4" of lead was used. All the lead bricks were assayed with the Geiger counter for their activity and only the ones with lower activity were chosen for the shielding around the setup.

Active Veto, Single Scatter Technique:

The outermost layer of CsI(Tl) in the 5 \times 5 setup was used for the active shielding/veto cut. This is termed as anti-coincidence



Figure 9: Schematic of the 3×3 prototype assembly of 9 CsI(Tl) crystals attached to EMI Photomultiplier tubes all on the same side for the search of Axions/ALPs at the reactor. The detector is hermetically shielded with 4" of lead, 1/4" of copper and water bricks to reduce the background [33].

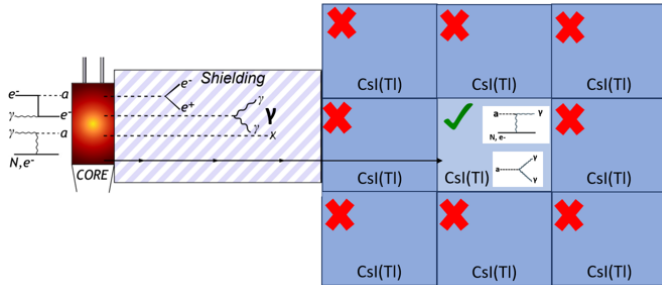


Figure 10: Schematic of the 3×3 prototype assembly of 9 CsI(Tl) crystals demonstrating the self-shielding or single scatter veto technique using the outer layer of CsI(Tl) for background reduction [33].

cut in all the plots mentioned in the paper. The anti-coincidence or single scatter cuts are implemented in offline analysis of data

Fig. 10 illustrates the single-scatter technique for a 3×3 detector setup. The center detector is designated as the main detector, while the surrounding eight detectors serve as the active veto. A $10\mu s$ coincidence window is selected for each event detected in the main detector. If any signal is detected in the veto detectors within this window, the event is excluded from the potential ALP signal because such a coincidence is highly unlikely for an ALP interaction and is therefore considered background. If no signal is detected in the veto detectors within this window, the event is included in the potential signal spectrum or single-scattered energy spectrum. This procedure is also applied to the 5×5 setup, where the inner 3×3 array is treated as a single detector, summing the energies of all nine central detectors while applying the single scatter cut technique.

3.5. Data Acquisition

For data acquisition, we have used a VME-based CAEN V1740D digitizer which is a 30 MHz analog-to-digital converter with 64-channels, 12-bit resolution, and 62.5 MS/s sampling rate with DPP-QDC (Digital Pulse Processing - Charge to

Digital Converter) firmware which can process the input pulses to produce integral (energy) and trigger time stamps for each event in the detector.

4. Results and Analysis

The experiment was built in phases starting with a prototype setup involving 9 CsI(Tl) crystals closely packed in a 3×3 geometry and then moving to 25 CsI(Tl) crystals with a 5×5 geometry. The center crystal is used for studying the single scatter events while the rest 8 crystals surrounding the center crystal are used as a veto for the center crystal making the fiducial mass as 3.5 kg and in the later case inner 9 crystals make 31.5 kg fiducial mass and the surrounding 16 crystals act as a veto. This assembly is hermetically shielded from all the sides with 4" of lead to suppressing external γ -rays, 1/4" of copper to stop low-energy x-rays and water bricks to control neutrons as already mentioned [33].

4.1. Prototype 3×3 CsI(Tl) Setup

The data was taken for this prototype set-up with the addition of all the shielding mentioned above. The experiment was moved closer to the reactor at a distance of approximately 4 meters, which gives us a good rate enhancement. The spectrum obtained using this modified 3×3 CsI(Tl) setup for reactor-on and off is shown in Fig. 11.

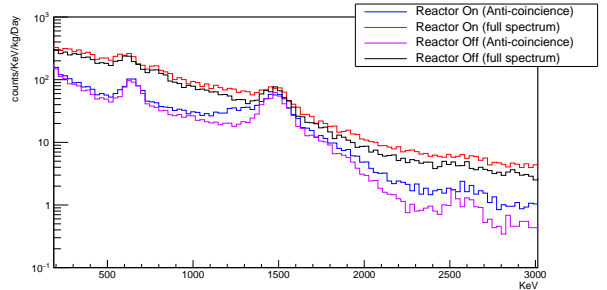


Figure 11: Comparison of reactor-on and off data for the center detector in 3×3 setup with and without the anti-coincidence (single scatter) cut [33].

We then added an additional layer of fresh air purge (shown in Fig.12) to the shielding around the 3×3 prototype assembly. The air-purge system is made of 3/16 inch acrylic material, covering all sides with small openings for wiring and venting fresh air at the bottom, and an inlet at the top for fresh air supplied by the air-compressor system at the NSC. This air-purge system is positioned outside the lead shielding and helps reduce airborne deposition of radioactive ^{41}Ar , which is activated by reactor neutrons and emits gamma radiation with an energy of 1.29 MeV. We observe an excess in the background spectrum around 1.29 MeV only when the reactor is on. The reduction in the gamma background due to ^{41}Ar decay, achieved using the fresh air-purge system, is clearly seen around the 1.29 MeV region in Fig.13.

We also compared the background spectrum of 3×3 set-up to the simulation spectrum. The background information for the



Figure 12: 3 × 3 setup with different layer of shielding [33].

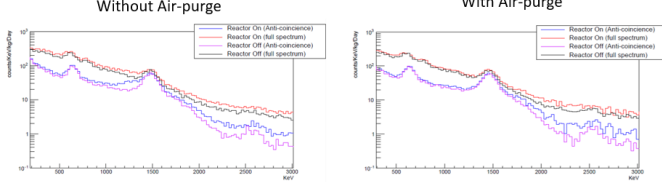


Figure 13: (Left) Reactor on and off comparison for the 3 × 3 setup without air purge. Excess at around 1.29 MeV in the reactor-on anti-coincidence can be seen due to ^{41}Ar . (Right): Reactor on and off comparison for the 3 × 3 setup with air purge. 1.29 MeV gamma is reduced in this plot due to the air-purge system [33].

experiment was simulated using SNOLAB background gamma spectrum from three sources: Uranium, Thorium, and Neutrons. This was used to simulate the expected external background. The gammas were generated in an isotropic manner from the surface of a sphere surrounding the 3 × 3 detector geometry. The Fig.14 shows matching results of experimental data with the simulation [33].

4.2. 5 × 5 CsI(Tl) Setup

After successful experiment for 3 × 3 set-up, we built another assembly of 25 crystal in 5 × 5 geometry (Fig.15) increasing the fiducial mass to 31.5 Kg from 3.5 kg. Same procedure were followed in terms of shielding, electronics, data acquisition and data analysis. Thermal cooling also provided to the

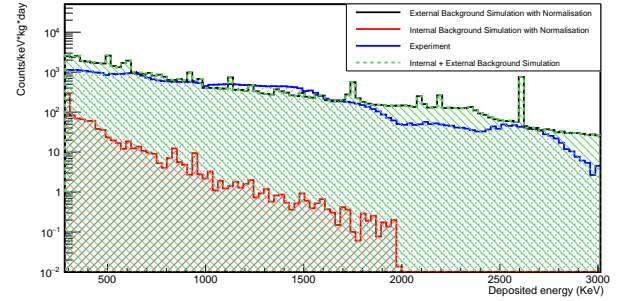


Figure 14: Comparison plot of simulated results with experiment. The y-axis is in DRU (differential-rate-unit). The x-axis is the energy deposited within the central CsI(Tl) crystal for a 3 × 3 geometry [33].



Figure 15: Different layers of the 5 × 5 CsI(Tl) setup consisting of 25 CsI(Tl) crystals attached to EMI photomultiplier tubes and voltage dividing circuit bases. The setup is hermetically shielded with 4" of lead [33].

set-up to cool down the PMT which gets damaged due to the heating issue. The reactor on and off spectrum for the 5 × 5 CsI(Tl) setup is shown in Fig. 16.

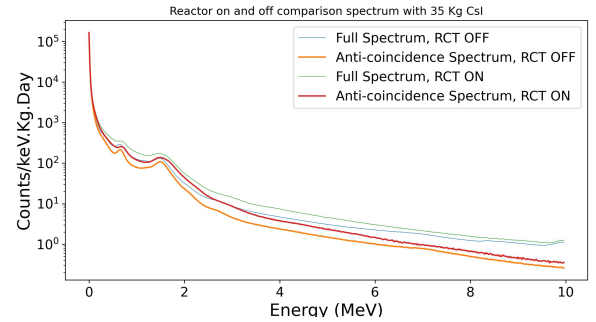


Figure 16: Reactor on and off background obtained using the 5×5 CsI(Tl) setup. Sub-100 DRU background along with reactor on/off differentiating capability is shown above 2 MeV region.

Fig. 16 shows the reactor on and off energy spectrum for the combined 3 × 3 center CsI(Tl) crystals with 31.5 Kg fiducial volume in the 5 × 5 assembly. Thin lines corresponds to the full spectrum, whereas thick lines corresponds to single-scattered (anti-coincidence) energy spectrum. The Single scatter technique (active veto) improves the background by a factor of two - three compared to the full energy spectrum. With this setup, we have achieved a background count of around 10-0.1 DRU in the energy range of 2-10 MeV as shown in Fig. 16 [33].

5. Conclusion And Experimental Reach

Fig. 17 shows the comparison of the sensitivity plot (m_a , $g_{a\gamma\gamma}$) and exclusion plot for the current 5×5 setup with ~ 30 kg fiducial volume and different exposure times. The flat limit for $m_a \leq 4 \times 10^4$ eV is due to the inverse Primakoff scattering which is a forward scattering in the detector with very small momentum transfer for small ALP masses whereas the limit peaked later is due to the $a \rightarrow \gamma\gamma$ decay rate which depends on the decay width as shown in Eq. 2 and the distance from the source. Due to the reactor photon flux quickly falling to zero by $E_\gamma \approx 10$ MeV, there is a sharp loss in sensitivity by $m_a \approx 10$ MeV[39].

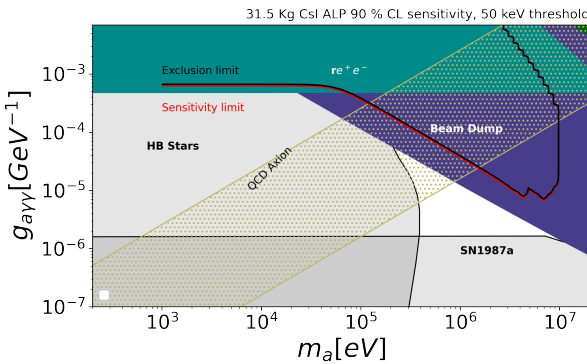


Figure 17: Exclusion plot drawn with the current experimental results. Red lines show the contour region for the sensitivity of the experiment and the blue line shows the contour region for the excludes region after the experimental data being collected for around 5 days.

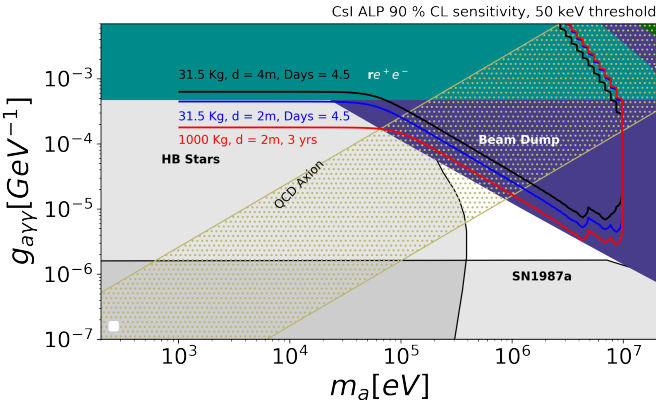


Figure 18: Projected sensitivity of the axion-electron coupling for CsI(Tl) detector. Black line is the current sensitivity, blue is the sensitivity with taking the detector as close as 2m to the reactor core. And the red line corresponds to the future modified generation of the experiment which considers scaling of the detector from 35 kg fiducial mass to 1000 kg fiducial mass.

Other astrophysical constraints are derived from SN1987a and horizontal branch (HB) stars [40, 41, 42, 43, 44, 45]. Lab-based limits are provided by the beam-dump and collider experiments for high-mass ALPs and low-mass ALP limit is provided by CAST and SUMICO [46]. Fig. 18 shows the projected sensitivity of the current experiment in the future. As seen from the

figure, we will be probing the experimentally unexplored astrophysical region just by taking the detector in close proximity to the reactor core (2 m). Also with scaling the detector size to 1000 kg and data taking time to 3 yrs we are inching towards the region of cosmological triangle [33].

6. Acknowledgements

The work presented in this thesis has been supported by LANL - TRIAD and DOE Grant Nos DE-SC0020097, DE-SC0018981, DESC0017859, and DE-SC0021051. We also acknowledge Mitchell Institute and the Nuclear Science and Engineering Center for providing institutional support with lab space and other required facilities to carry out experimentation.

References

- [1] F. Zwicky, Die Rotverschiebung von extragalaktischen Nebeln, *Helv. Phys. Acta* 6 (1933) 110–127. doi:10.1007/s10714-008-0707-4.
- [2] F. Zwicky, 107. On the Masses of Nebulae and of Clusters of Nebulae, Harvard University Press, Cambridge, MA and London, England, 1979, pp. 729–737 [cited 2024-05-27]. doi:doi:10.4159/harvard.9780674366688.c115. URL <https://doi.org/10.4159/harvard.9780674366688.c115>
- [3] V. C. Rubin, J. W. K. Ford, Rotation of the andromeda nebula from a spectroscopic survey of emission regions, *Astrophys. J.* 159 (1970) 379–403.
- [4] C. Alcock, C. W. Akerlof, R. Allsman, T. Axelrod, D. Bennett, S. Chan, K. Cook, K. C. Freeman, K. Griest, S. L. Marshall, et al., Possible gravitational microlensing of a star in the large magellanic cloud, *nature* 365 (6447) (1993) 621–623.
- [5] K. Zioutas, C. Aalseth, D. Abriola, F. Avignone Iii, R. Brodzinski, J. Collar, R. Creswick, D. Di Gregorio, H. Farach, A. Gattone, et al., A decommissioned lhc model magnet as an axion telescope, *Nuclear Instruments and Methods in Physics Research Section A: Accelerators, Spectrometers, Detectors and Associated Equipment* 425 (3) (1999) 480–487.
- [6] V. Anastassopoulos, S. Aune, K. Barth, A. Belov, G. Cantatore, J. Carmona, J. Castel, S. Cetin, F. Christensen, J. Collar, et al., New cast limit on the axion-photon interaction, *arXiv preprint arXiv:1705.02290* (2017).
- [7] I. G. Irastorza, F. Avignone, A. Liolios, S. Russenschuck, H. t. Kate, K. van Bibber, T. Geralis, O. Limousin, J. Villar, H. Gomez, et al., The international axion observatory iaxo. letter of intent to the cern sps committee, *Tech. rep.* (2013).
- [8] Y. Kahn, B. R. Safdi, J. Thaler, Broadband and resonant approaches to axion dark matter detection, *Physical review letters* 117 (14) (2016) 141801.
- [9] C. P. Salemi, First results from abracadabra-10cm: a search for low-mass axion dark matter, *arXiv preprint arXiv:1905.06882* (2019).
- [10] S. Asztalos, E. Daw, H. Peng, L. Rosenberg, C. Hagnann, D. Kinion, W. Stoeffl, K. van Bibber, P. Sikivie, N. Sullivan, et al., Large-scale microwave cavity search for dark-matter axions, *Physical Review D* 64 (9) (2001) 092003.
- [11] N. Du, N. Force, R. Khatiwada, E. Lentz, R. Ottens, L. Rosenberg, G. Rybka, G. Carosi, N. Woollett, D. Bowring, et al., Search for invisible axion dark matter with the axion dark matter experiment, *Physical review letters* 120 (15) (2018) 151301.
- [12] D. Kimball, S. Afach, D. Aybas, J. Blanchard, D. Budker, G. Centers, M. Engler, N. Figueroa, A. Garcon, P. Graham, et al., Overview of the cosmic axion spin precession experiment (casper), *arXiv preprint arXiv:1711.08999* (2017).
- [13] B. M. Brubaker, et al., First results from a microwave cavity axion search at 24 μ eV, *Phys. Rev. Lett.* 118 (6) (2017) 061302. arXiv:1610.02580, doi:10.1103/PhysRevLett.118.061302.
- [14] A. G. Droster, K. van Bibber, Haystac status, results, and plans, *arXiv preprint arXiv:1901.01668* (2019).
- [15] A. Spector, ALPSII Status Report, in: 14th Patras Workshop on Axions, WIMPs and WISPs, 2019. arXiv:1906.09011.

- [16] A. C. Melissinos, Search for cosmic axions using an optical interferometer, arXiv preprint arXiv:0807.1092 (2008).
- [17] W. DeRocco, A. Hook, Axion interferometry, Physical Review D 98 (3) (2018) 035021.
- [18] H. Liu, B. D. Elwood, M. Evans, J. Thaler, Searching for axion dark matter with birefringent cavities, Physical Review D 100 (2) (2019) 023548.
- [19] I. Obata, T. Fujita, Y. Michimura, Optical ring cavity search for axion dark matter, Physical review letters 121 (16) (2018) 161301.
- [20] J. L. Feng, I. Galon, F. Kling, S. Trojanowski, Axionlike particles at faser: The lhc as a photon beam dump, Physical Review D 98 (5) (2018) 055021.
- [21] A. Berlin, N. Blinov, G. Krnjaic, P. Schuster, N. Toro, Dark matter, millicharges, axion and scalar particles, gauge bosons, and other new physics with ldmx, Physical Review D 99 (7) (2019) 075001.
- [22] T. Åkesson, A. Berlin, N. Blinov, O. Colegrove, G. Collura, V. Dutta, B. Echenard, J. Hiltbrand, D. G. Hitlin, J. Incandela, et al., Light dark matter experiment (ldmx), arXiv preprint arXiv:1808.05219 (2018).
- [23] R. Volpe, Search for exotic decays at na62, arXiv preprint arXiv:1910.10429 (2019).
- [24] A. Berlin, S. Gori, P. Schuster, N. Toro, Dark sectors at the fermilab seaquest experiment, Physical Review D 98 (3) (2018) 035011.
- [25] S. Alekhin, W. Altmannshofer, T. Asaka, B. Batell, F. Bezrukov, K. Bonnarenko, A. Boyarsky, K.-Y. Choi, C. Corral, N. Craig, et al., A facility to search for hidden particles at the cern sps: the ship physics case, Reports on Progress in Physics 79 (12) (2016) 124201.
- [26] W. M. Bonivento, D. Kim, K. Sinha, Passat: particle accelerator helioscopes for slim axion-like-particle detection, The European Physical Journal C 80 (2) (2020) 164.
- [27] E. Aprile, J. Aalbers, F. Agostini, M. Alfonsi, L. Althueser, F. Amaro, V. C. Antochi, E. Angelino, J. Angevaare, F. Arneodo, et al., Excess electronic recoil events in xenon1t, Physical Review D 102 (7) (2020) 072004.
- [28] J. B. Dent, B. Dutta, J. L. Newstead, A. Thompson, Inverse primakoff scattering as a probe of solar axions at liquid xenon direct detection experiments, Physical Review Letters 125 (13) (2020) 131805.
- [29] T. Aralis, T. Aramaki, I. J. Arnquist, E. Azadbakht, W. Baker, S. Banik, D. Barker, C. Bathurst, D. Bauer, L. Bezerra, et al., Constraints on dark photons and axionlike particles from the supercdms soudan experiment, Physical Review D 101 (5) (2020) 052008.
- [30] C. Fu, X. Zhou, X. Chen, Y. Chen, X. Cui, D. Fang, K. Giboni, F. Giuliani, K. Han, X. Huang, et al., Limits on axion couplings from the first 80 days of data of the pandax-ii experiment, Physical Review Letters 119 (18) (2017) 181806.
- [31] J. B. Dent, B. Dutta, D. Kim, S. Liao, R. Mahapatra, K. Sinha, A. Thompson, New directions for axion searches via scattering at reactor neutrino experiments, Physical Review Letters 124 (21) (2020) 211804.
- [32] M. Collaboration, G. Agnolet, W. Baker, D. Barker, R. Beck, T. J. Carroll, J. Cesar, P. Cushman, J. B. Dent, S. D. Rijck, B. Dutta, W. Flanagan, M. Fritts, Y. Gao, H. R. Harris, C. C. Hays, V. Iyer, A. Jastram, F. Kadribasic, A. Kennedy, A. Kubik, I. Ogawa, K. Lang, R. Mahapatra, V. Mandic, R. D. Martin, N. Mast, S. McDeavitt, N. Mirabolfathi, B. Mohanty, K. Nakajima, J. Newhouse, J. L. Newstead, D. Phan, M. Proga, A. Roberts, G. Rogachev, R. Salazar, J. Sander, K. Senapati, M. Shimada, L. Strigari, Y. Tamagawa, W. Teizer, J. I. C. Vermaak, A. N. Villano, J. Walker, B. Webb, Z. Wetzel, S. A. Yadavalli, Background studies for the miner coherent neutrino scattering reactor experiment (2016). [arXiv:1609.02066](https://arxiv.org/abs/1609.02066).
- [33] S. D. Verma, Fabrication of cdms dark matter detector using bi-layer lift-off technique and detection of axions/axion like particles (alps) using csi(tl) scintillator detectors, Ph.D. thesis, Texas A-M (2022).
- [34] M. Roos, Sources of gamma radiation in a reactor core, Journal of Nuclear Energy. Part B. Reactor Technology 1 (2) (1959) 98–104.
- [35] D. A. Sierra, V. De Romeri, L. J. Flores, D. Papoulias, Axionlike particles searches in reactor experiments, Journal of High Energy Physics 2021 (3) (2021) 1–38.
- [36] L. Waites, A. Thompson, A. Bungau, J. M. Conrad, B. Dutta, W.-C. Huang, D. Kim, M. Shaevitz, J. Spitz, Axionlike particle production at beam dump experiments with distinct nuclear excitation lines, Physical Review D 107 (9) (2023) 095010.
- [37] G. Heusser, Low-radioactivity background techniques, Annual Review of Nuclear and Particle Science 45 (2003) 543–590. doi:10.1146/annurev.ns.45.120195.002551.
- [38] T. Kim, I. Cho, D. Choi, J. Choi, I. Hahn, M. Hwang, H. Jang, R. Jain, U. Kang, H. Kim, et al., Study of the internal background of csi ($t\ell$) crystal detectors for dark matter search, Nuclear Instruments and Methods in Physics Research Section A: Accelerators, Spectrometers, Detectors and Associated Equipment 500 (1-3) (2003) 337–344.
- [39] J. B. Dent, B. Dutta, D. Kim, S. Liao, R. Mahapatra, K. Sinha, A. Thompson, New directions for axion searches via scattering at reactor neutrino experiments, Physical Review Letters 124 (21) (5 2020). doi:10.1103/PhysRevLett.124.211804.
- [40] J. W. Brockway, E. D. Carlson, G. G. Raffelt, Sn 1987a gamma-ray limits on the conversion of pseudoscalars, Physics Letters B 383 (4) (1996) 439–443. doi:[https://doi.org/10.1016/0370-2693\(96\)00778-2](https://doi.org/10.1016/0370-2693(96)00778-2). URL <https://www.sciencedirect.com/science/article/pii/0370269396007782>
- [41] G. G. Raffelt, Astrophysical axion bounds diminished by screening effects, Phys. Rev. D 33 (1986) 897–909. doi:10.1103/PhysRevD.33.897. URL <https://link.aps.org/doi/10.1103/PhysRevD.33.897>
- [42] G. G. Raffelt, D. S. P. Dearborn, Bounds on hadronic axions from stellar evolution, Phys. Rev. D 36 (1987) 2211–2225. doi:10.1103/PhysRevD.36.2211. URL <https://link.aps.org/doi/10.1103/PhysRevD.36.2211>
- [43] A. Ayala, I. Domínguez, M. Giannotti, A. Mirizzi, O. Straniero, Revisiting the bound on axion-photon coupling from globular clusters, Phys. Rev. Lett. 113 (2014) 191302. doi:10.1103/PhysRevLett.113.191302. URL <https://link.aps.org/doi/10.1103/PhysRevLett.113.191302>
- [44] P. Carenza, O. Straniero, B. Döbrich, M. Giannotti, G. Lucente, A. Mirizzi, Constraints on the coupling with photons of heavy axion-like-particles from globular clusters, Physics Letters B 809 (2020) 135709. doi:<https://doi.org/10.1016/j.physletb.2020.135709>. URL <https://www.sciencedirect.com/science/article/pii/S0370269320305128>
- [45] G. Lucente, P. Carenza, T. Fischer, M. Giannotti, A. Mirizzi, Heavy axion-like particles and core-collapse supernovae: constraints and impact on the explosion mechanism, Journal of Cosmology and Astroparticle Physics 2020 (12) (2020) 008–008. doi:10.1088/1475-7516/2020/12/008. URL <https://doi.org/10.1088/1475-7516/2020/12/008>
- [46] D. Aristizabal Sierra, V. De Romeri, L. J. Flores, D. K. Papoulias, Axionlike particles searches in reactor experiments, JHEP 03 (2021) 294. arXiv:2010.15712, doi:10.1007/JHEP03(2021)294.